Effects of mixing chamber length, feedback channel head loss and nozzle-to-plate distance on sweeping jets impingement heat transfer

Cristina D'Angelo[1*]

[1*]Department of Industrial Engineering, University of Naples "Federico II", via Claudio 21, Naples, 80025, Italy.

Corresponding author E-mail: cristina.dangelo@unina.it;

Abstract

The convective heat transfer performances of sweeping jets impinging on a heated thin foil are experimentally investigated. The analysis is performed by employing the Infrared Thermography technique coupled with the heated thin foil heat flux sensor. Two sweeping jet devices, characterized by different mixing chamber lengths, are employed and their heat transfer performances are evaluated for non-dimensional nozzle-to-plate distances H/w ranging between 2 and 10. Furthermore, in order to analyse different head losses conditions, the geometry of the feedback channels of the device characterized by the longest mixing chamber length has been varied. In particular, the non-dimensional parameter g/w, which represents the dimensionless minimum passage area of the feedback channel, has been introduced; six different values of g/w have been taken into account (g/w = 1, 0.83, 0.67, 0.50, 0.33, and 0.17). Time-averaged and phase-averaged analyses have been carried out in order to characterize the heat transfer behaviour of the sweeping jet devices and highlight the influence of the nozzle-to-plate distance, of the mixing chamber length and of the feedback channel head loss on such behaviour. This work shows that an excessive reduction of the mixing chamber length causes the suppression of the jet oscillation and a consequent variation in the Nusselt number distribution; furthermore, the convective heat transfer interests a wider area of the target plate as the the nozzle-to-plate distance increases while the opposite trend is observed by increasing the head losses.

Keywords: Sweeping jets, impingement heat transfer, influence of geometric parameters

1 Introduction

Sweeping jet fluidic oscillators are devices which convert a steady jet into an oscillating jet due to intrinsic flow instability mechanisms and without requiring any moving parts, piezo-electrical or electromechanical elements [1]. Because of their simplicity, reliability, and low maintenance costs, the interest in fluidic oscillators has remarkably grown over the last few years, especially for active flow control purposes [2], for applications in the field of heat transfer and in applications such as gas turbine, electronic devices, and metallurgy [3,4]. Fluidic oscillators are, in fact, small, do not contain any moving parts and are capable of exerting high momentum. The oscillations are entirely self-induced and self-sustaining [2].

In order to obtain an efficient convective heat transfer over a surface, arrays of stationary jets are required, owing to their limited region of influence, which is centred on the impacted region. The increased penalty in pressure loss, typical of the application of arrays of stationary jets, is one of the main reasons which motivates researchers to explore alternative impingement strategies, such as sweeping jets [5–7]. Indeed, sweeping jets can extend the spatial region of impingement flow and are characterized by a more efficient convective heat transfer with respect to the performances of conventional circular jets [8].

Despite the technology of fluidic oscillators was developed more than 50 years ago, these devices have mostly been used with liquids as working fluid [9], for applications like sprinklers, shower heads, and Jacuzzis. Recent research on separation control [10], noise reduction [11], combustion control [12], and film cooling [13] employed air and other gases as a working fluid.

It is then possible to comprehend that understanding the internal dynamics of fluidic oscillators and the external properties of oscillating jets is of crucial interest for a wide range of possible applications.

Several actuator designs have been proposed. Three main categories are suggested in [14]: feedback-free oscillators, oscillators with one feedback channel and oscillators with two feedback channels. The design with two feedback channels [15], as shown in Figure 1, is the most popular [16,17].

With reference to Figure 1, the fluid supply (1) is the inlet section where the air mass flows into the oscillator. The power nozzle (2) connects the air supply to the mixing chamber (4). The feedback channels (3) are the fundamental parts of the fluidic oscillator; they link the last section of the mixing chamber to the exit of the power nozzle. The control port (5) is the part where the flow that comes from the feedback channel mixes with the main flow from the power nozzle. Lastly, the flow exits the oscillator from the outlet nozzle (6). As a consequence of the interaction between the jet in the mixing chamber and the jet from the feedback channels, the jet oscillates between the two most deflected positions in the external flow field domain.

The fluid dynamic behaviour behind the sweeping motion of the issued jet is depicted in Figure 2. For $\phi = 0°$ the flow emanating from the power nozzle enters the mixing chamber. The flow touching the entrance wedges, causes the generation of a recirculation region in the left feedback channel. In
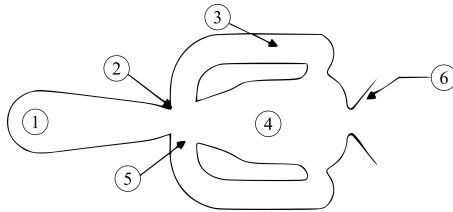
Fig. 1: Scheme of a fluidic oscillator with two feedback channels. The figure highlights the main components: fluid supply (1), power nozzle (2), feedback channel (3), mixing chamber (4), control port (5) and outlet (6).

the downstream area two recirculation bubbles are generated, the right one pushes the jet off the wall, while the left one remains between the jet and the left sidewall. At this stage the flow is attached to the left sidewall due to the Coanda effect; as the flow develops through the fluidic oscillator, some fluid passes through the throat section and attaches to the diverging nozzle surface opposite to the sidewall where the Coanda effect occurs. The remaining fluid enters the left feedback channel and moves upstream to the exit section of the feedback channel, near the power nozzle, and interacts with the main jet at the entry of the mixing chamber producing the growth of the left recirculation bubble and its propagation downstream ($\phi = 60°$). Consequently, the left recirculation bubble pushes the jet off the wall moving it toward the right sidewall ($\phi = 120°$) to which the flow attaches again, due to the Coanda effect ($\phi = 180°$). The growing recirculation region bends the main jet to the other sidewall of the oscillator, making the jet sweep from one sidewall to another. This process repeats cyclically [18] and occurs in time with a certain frequency, generating a sweeping jet exiting the diverging nozzle of the fluidic oscillator.
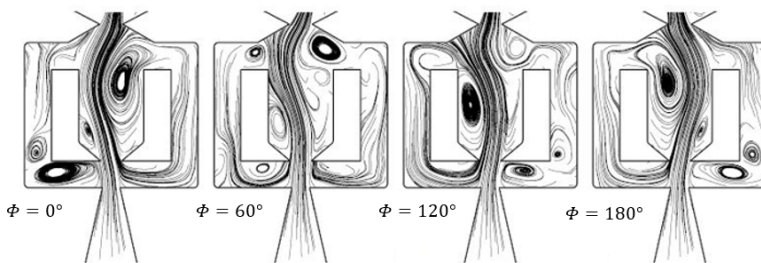

Fig. 2: Sweeping oscillation mechanism (ϕ is the phase angle of the jet oscillation period) [16].

Depending on the actuator's geometry, size and supplied flowrate, the oscillation frequency may be of the order of 10 Hz [18] up to the order of 20 kHz [19]. Furthermore, as shown in [12,19], the oscillation frequency is proportional to the supplied flowrate.

Some experimental studies and numerical simulations have focused on the influence of some geometrical parameters of fluidic oscillators on the flow field characteristics of free sweeping jets [1, 2, 15]. Differently, lower attention has been paid to their impinging flow field and to the influence of such geometrical parameters on the heat transfer performances of sweeping jets.

In [20] sweeping jets created by a conventional feedback-type fluidic oscillator are investigated; two different values of the exit nozzle angle were considered, 70° and 102°. For $H/w = 6$ it was found that the device with a 70° exit nozzle angle provides heat transfer at higher distances along the direction of the oscillation due to a wider spread of the jet, but the device with a 102° exit nozzle angle has a greater heat transfer at the impingement centre.

In [8] experiments were conducted to evaluate the heat transfer performances of a sweeping jet impinging at non dimensional nozzle-to-plate distances $H/w = 0.5, 1.0, 2.0$ and 3.0. It was found that as H/w increases, the heat transfer patterns begin to elongate along the direction of the oscillation, resulting in a much wider influenced region compared to the one obtained at $H/w = 0.5$. Furthermore, it has been observed that the heat transfer performances are significantly reduced as H/w increases; indeed, owing to the oscillation of the sweeping jet, because of the increase of H/w the jet is able to cover a larger region of the impinged plate, but the impingement velocity greatly decreases as H/w increases.

The limited knowledge about the effects of the geometrical characteristics of the sweeping jet device on its heat transfer performance is the motivation behind this work, the aim of which is to assess the influence of the nozzle-to-plate distance, of the mixing chamber length and of the feedback channel head loss on the heat transfer performances of impinging sweeping jets through time-averaged and phase-averaged analyses.

2   Experimental setup

In the current section the experimental setup, the operating conditions and the design of the fluidic oscillators employed in the experiments performed are described.

2.1   Experimental apparatus and operating conditions

The experimental apparatus is schematically shown in Figure 3.

The air flow that passes through the fluidic oscillator is generated by a centrifugal blower; an inverter is used to regulate the input shaft power. The frequency of the inverter is set to 34.5 Hz; the volume flow rate Q_v, which is measured using a flow meter, is equal to 2.6 NL/s. Hence, the Reynolds number is obtained as written in Equation 1:

$$Re = \frac{4Q_v}{\nu\pi w} = 2.16 \times 10^4 \qquad (1)$$

where ν is the kinematic viscosity of the air and w is the hydraulic diameter of the fluidic oscillator, equal to the width of the throat section.

The test environment is characterized by a temperature of about 27-28 °C and a pressure of about 101-102 kPa. All the experiments are performed at the same value of the Reynolds number.

In the experimental apparatus employed, the air flow supplied by the blower moves through a heat exchanger, in order to keep the air temperature equal to the ambient one. Subsequently, the air passes through the flow meter and into a plenum chamber, which is internally equipped with two honeycomb grids that break the vortical structures generated upstream of the chamber itself, in order to reduce the turbulence naturally occurring across the chamber and therefore to provide homogeneous inflow conditions. The fluidic oscillator is connected to the plenum chamber; the flow comes out from the fluidic oscillator and impinges the thin foil on its bottom face. The fluidic oscillator is mounted on a translation stage in order to allow the variation of the nozzle-to-plate spacing H with an accuracy of 0.5 mm. The impingement plate is horizontally positioned by using four fixed supports which do not confine the oscillation of the jet. The exit section of the fluidic oscillator is placed at a distance H from the impingement plate itself; the sweeping jet impinges vertically from below.

For the performed analysis, the non-dimensional nozzle-to-plate distance H/w ranges between 2 and 10.

The temperature distribution over the thin foil is measured by using an IR camera which looks at the face of the foil opposite to the side where the jet impinges.
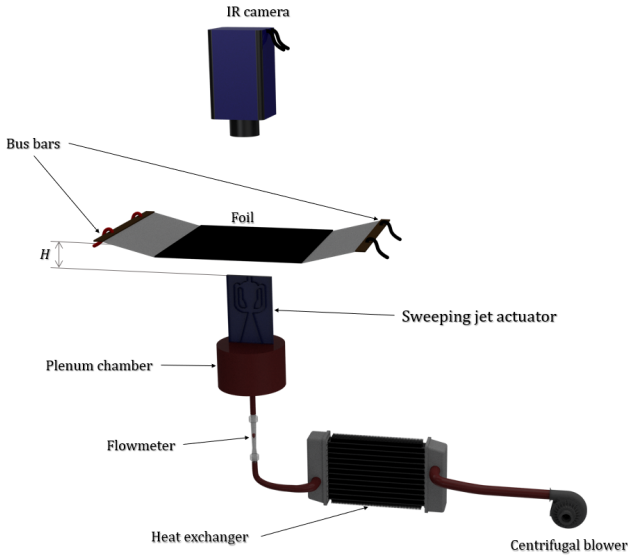

Fig. 3: Schematic of the experimental apparatus.

The impingement plate is a constantan foil and is 200 mm wide, 450 mm long and 50 μm thick. The foil is steadily and uniformly heated by Joule effect,

and it is cooled by the sweeping jet impinging on it. The Joule heating of the foil is obtained by applying a constant voltage across it with the aid of a stabilized DC power supply and two couples of bus bars, made of copper, clamped at the shortest sides of the foil. The large equivalent cross section (weighted with the electrical resistivity) of the bus bars, with respect to that of the heated foil, ensures negligible voltage drop through them. The electrical contact between the bus bars and the foil is enhanced by using an indium wire (about 0.5 mm in diameter). The foil rear surface is coated with a high emissivity paint (hemispherical emissivity $\varepsilon = 0.95$) in order to increase the accuracy of the temperature measurements.

The IR camera measures the foil surface temperature with a spatial resolution of 2.48 pixels/mm; for the current experiments an IR camera CEPID JADE III with a focal plane array of 320x240 is used.

The camera is accurately calibrated with a blackbody for the whole measurement range, with the temperature of the blackbody ranging between 36 °C and 42 °C with a spacing of 3 °C. The noise equivalent temperature level of the camera is about 25 mK, and the RMS error from the blackbody calibration is less than 0.1 K.

In order to analyse the variation of the convective heat transfer on the impingement plate, the IR camera sampling frequency f_{IR} is set to 125 Hz by using a trigger signal sent to the camera by a pulse generator; the integration time is set to 520 µs. 5000 images are acquired for each test; the first 500 images are discarded in order to take into account the camera stabilisation period. The duration of each test is equal to 40 s.

In order to perform the phase averaged analysis, it is necessary to identify the phase of the temperature snapshots in the sweeping oscillation and, thus, to measure a property of the flow in a time-resolved manner; for this purpose, the pressure drop across one feedback channel is measured by using a differential pressure transducer connected to two pressure taps located at the centre of the feedback channel inlet and outlet sections. The sampling frequency of the pressure signal f_s is 10 kHz, therefore 400000 samples are acquired during each test. It is crucial for the experiment that the IR Camera trigger signal and the instantaneous pressure signal are acquired simultaneously.

2.2 Design of the fluidic oscillator

The fluidic oscillators investigated in the present work have been made with a 3D Printer.

Figure 4 shows the drafting of the oscillators employed in the experimental campaign.

The shapes of the devices are referred to the model of the fluidic oscillator described by Horne et al. [21]. The actuators consist of two parts symmetrical with respect to the plane of oscillation of the jet, glued and then screwed together.

Two devices with similar internal geometry have been tested. All the characteristic dimensions of the devices have been designed and scaled with respect
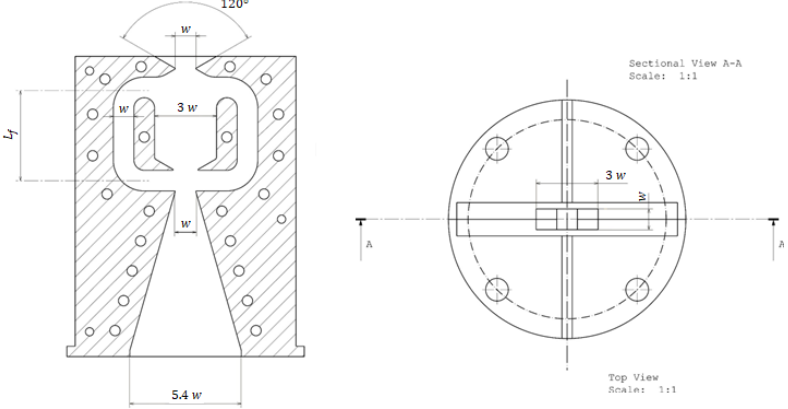
Fig. 4: Draft of the fluidic oscillator, front view and top view.

to a reference length, which has been chosen to be the edge of the squared exit nozzle throat, $w = 10\,\text{mm}$; the reference area is $A_{ref} = 100\ \text{mm}^2$. Both the devices employed in the experimental campaign have a width of the feedback channels equal to w and a spreading angle of the exit nozzle of 120°. The aspect ratio AR of both the devices, defined as the ratio between the throat height and the throat width, is equal to 1. The length of the mixing chamber L_f of the two investigated fluidic oscillators is equal to $2.5w$ and $4.5w$; L_f is here defined as the distance between the centre of the feedback channel exit and enter sections, as shown in Figure 4.

In order to analyse the effect of the minor head losses on the heat transfer performances of fluidic oscillators, the device with the longest mixing chamber length has also been provided with tapped holes on its shortest sides, in which it has been possible to fasten a screw to reduce the minimum passage section of the feedback channels. The parameter g/w has been introduced in order to express the effect of the minor head losses (see Figure 5). In particular, the investigated values of g/w are: $g/w = 1$, $g/w = 0.83$, $g/w = 0.67$, $g/w = 0.50$, $g/w = 0.33$, and $g/w = 0.17$. For $g/w = 1$, i.e. when the minimum passage area coincides with the width of the feedback channel, the minor head losses are absent, while the maximum minor head losses condition is characterized by $g/w = 0$, when the feedback channel is completely closed (this particular case has not been analysed in the current work).

3 Data reduction and analysis

The IR camera is used as a temperature transducer in conjunction with the heated thin foil sensor in order to determine the convective heat transfer coefficient h by applying a local energy balance to the foil. This method is known as heated thin foil technique, a widely documented technique in literature [22–24].
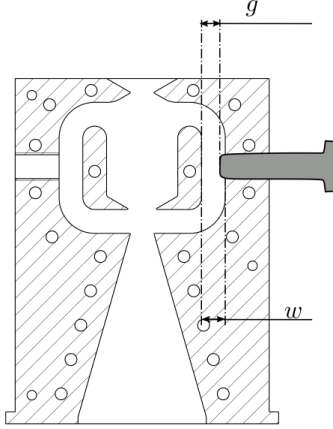
Fig. 5: g/w effect. Focus on the feedback channel section area.

By applying the energy balance to the foil, the convective heat transfer coefficient h, function of the spatial coordinates x and y and of the time t, can be evaluated as in Equation 2:

$$h(x,y,t) = \frac{\dot{q}_j - \dot{q}_r - \dot{q}_n - \dot{q}_k - \rho_{foil} c \delta \frac{dT_W}{dt}}{T_w - T_{aw}} \tag{2}$$

In Equation 2 $\dot{q}_j$ is the Joule heat flux, $\dot{q}_r$ the radiation heat flux, $\dot{q}_n$ the natural convection heat flux on the rear foil surface, $\dot{q}_k$ the tangential conduction heat flux, ρ_{foil} the constantan density, c the constantan specific heat, δ the foil thickness, dT_w/dt the time derivative of the wall temperature T_w, and T_{aw} is the adiabatic wall temperature.

Each experiment consists of two acquisitions: a "hot" acquisition with electric current on, during which the thin foil is heated by a measured $\dot{q}_j$, which allows to measure T_w, and a "cold" acquisition with electric current off, which provides T_{aw}. Furthermore, the temperature is considered constant through the foil thickness, because the Biot number ($Bi = \overline{h}\delta/\lambda_f$, being λ_f the foil thermal conductivity) and the inverse of the modified Fourier number ($Fo_f = \alpha/(\pi f \delta^2)$ where α is the foil thermal diffusivity) are small with respect to unity [25].

The time-averaged convective heat transfer coefficients are obtained by applying Equation 3, where the upper bar indicates the time-averaged quantities, evaluated as the average of all the 4500 acquired samples for the current experiments:

$$\overline{h}(x,y) = \frac{\dot{q}_j - \overline{\dot{q}}_r - \overline{\dot{q}}_n - \overline{\dot{q}}_k}{\overline{T_w} - \overline{T_{aw}}} \tag{3}$$

The phase-averaged convective heat transfer coefficients h_ϕ are determined from Equation 4 by replacing the instantaneous quantities with the corresponding phase-averaged ones (denoted by a hat):

$$h_\phi(x,y) = \frac{\dot{q}_j - \widehat{\dot{q}}_r - \widehat{\dot{q}}_n - \widehat{\dot{q}}_k - \rho_{foil}c\delta\frac{d\widehat{T_W}}{dt}}{\widehat{T_w} - \widehat{T_{aw}}} \tag{4}$$

The phase-averaged temperature can be expressed as the sum of the time-averaged temperature $\overline{T}$ and the phase organized fluctuation $\widetilde{T}$. The latter is a zero-mean periodic function of time that can be developed in Fourier series as follows:

$$\widetilde{T}(x,y,\phi) = \sum_{k=1}^{\infty} C_k \cos(k\phi) + S_k \sin(k\phi) \tag{5}$$

where the series coefficients C_k and S_k are computed from the following equations:

$$C_k(x,y) = \frac{2}{N} \sum_{1=1}^{N} (T_i - \overline{T}) \cos(k\phi_i) \tag{6}$$

$$S_k(x,y) = \frac{2}{N} \sum_{1=1}^{N} (T_i - \overline{T}) \sin(k\phi_i) \tag{7}$$

With N being the number of samples, i.e. 4500, T_i the generic temperature snapshots and ϕ_i the corresponding phase angle.

The phase ϕ_i is computed from the recorded pressure signal. For this purpose, the IR Camera trigger output signal and the instantaneous pressure signal are acquired simultaneously. As a first step, the most probable frequency of the sweeping oscillation f_0 is computed from the spectrogram of the pressure signal; afterwards, the phase angle corresponding to each snapshot is evaluated by fitting a sinusoid to the pressure signal restricted to a temporal window centred around the time of the snapshot acquisition and characterized by a duration equal to $1/f_0$. Once the phase distribution is known, the pseudo-Fourier modes C_k and S_k can be computed from Equation 6 and Equation 7. Then, Equation 5 is used to determine the phase-correlated fluctuation $\widetilde{T}$ and the phase-averaged temperature can be evaluated from the equation $\widehat{T} = \overline{T} + \widetilde{T}$. The computation of $\widetilde{T}$ implies truncation of the series in Equation 5. In the present measurements it was observed that coherent patterns of the phase-averaged temperatures are obtained by limiting the series to the second-order harmonics ($k = 2$). Therefore, only the first two couples of modes have been used to reconstruct $\widetilde{T}$. The phase-averaged balance in Equation 4 is applied to a number of phases chosen arbitrarily and equal to 60 in the present case.

In the following, data is reduced in the form of Nusselt number distribution, being the Nusselt number defined as in Equation 8:

$$Nu = \frac{hD}{\lambda} \tag{8}$$

where h is the convective heat transfer coefficient and λ is the air thermal conductivity.

4 Results

The aim of the current investigation is to analyse the heat transfer perfor-
mances of two sweeping jet devices, characterized by different mixing chamber
lengths, impinging on a thin foil, varying the non-dimensional nozzle-to-plate
distance H/w. For each device values of H/w equal to $2, 4, 6, 8$ and 10 have
been investigated. Furthermore, in order to investigate the effect of the head
loss on the convective heat transfer behaviour of the fluidic oscillator hav-
ing the longer mixing chamber length, the screws have been fastened into the
tapped holes of the device to reduce the section of the feedback channel.

A total of 30 different configurations obtained by combining the values of
H/w, L_f/w and g/w have been tested; for the device having $L_f/w = 2.5$ only
the parameter H/w has been varied.

This section aims to present the results in terms of the time-averaged $\overline{Nu}$
and phase-averaged Nusselt number Nu_ϕ. Since no significant phase-organized
fluctuations are computed for the case $L_f/w = 2.5$, phase-averaged results are
presented only for the device having $L_f/w = 4.5$. Indeed, as also found with
numerical simulations in [1], an excessive reduction of the mixing chamber
length causes the suppression of the jet oscillation.

In the following sections the effect of the nozzle-to-plate distance, of the
mixing chamber length and of the feedback channel head loss over the heat
transfer performances of impinging sweeping jets has been analysed.

4.1 Effects of the nozzle-to-plate distance

In the current section the effect of the nozzle-to-plate distance over the heat
transfer performances of impinging sweeping jets has been investigated.

Firstly, the configuration with $g/w = 1$ (i.e. absence of minor head losses)
for the device having $L_f/w = 4.5$ has been considered, varying the nozzle-to-
plate distance.

The oscillation frequency of the device characterized by $L_f/w = 4.5$ is
approximately equal to $50\,\text{Hz}$.

In the following figures the phase-averaged Nusselt number distribution
Nu_ϕ for H/w equal to 2 and 6 are illustrated for the sweeping jet device char-
acterized by $L_f/w = 4.5$. A sequence of 6 snapshots evenly spaced from each
other is extracted from 60 phase-averaged snapshots. The acquired snapshots
cover a complete oscillation cycle of the sweeping jet, with phase angles ranging
between $\phi = 0°$ and $\phi = 300°$, with a spacing of $60°$ from each other.

In Figure 6 the phase-averaged Nusselt number distribution Nu_ϕ for 6
phases at the nozzle-to-plate distance $H/w = 2$ is depicted.

In the Nu_ϕ maps at $H/w = 2$ a well-defined spot of the maximum convec-
tive heat transfer can be seen, due to the small distance between the exit nozzle
and the plate. The Nu_ϕ takes a minimum value at the foil edges and reaches
its maximum value at the impingement centre, differently from the cases at
higher H/w, where the maximum Nu_ϕ is reached far from the impingement
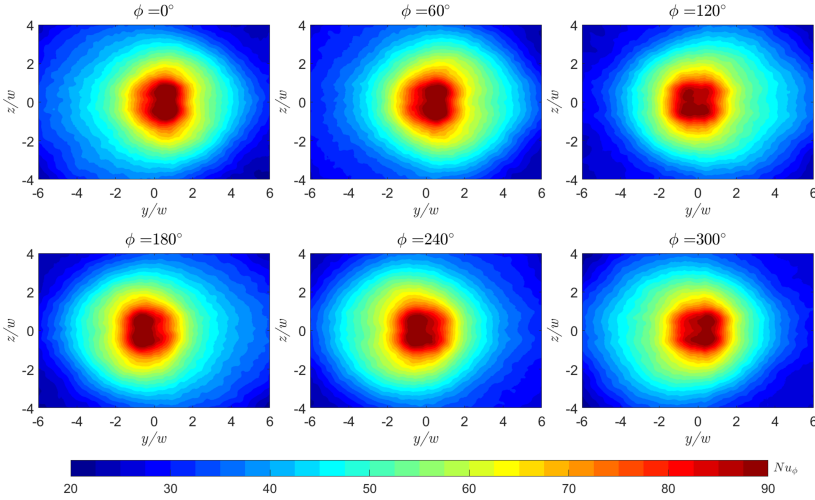centre, due to a larger spread of the jet.

Fig. 6:   Phase-averaged Nusselt number maps for $H/w = 2$, $L_f/w = 4.5$, $Re = 2.16 \times 10^4$.

Due to the small distance from the plate, it is not possible to visualize a clear oscillation of the sweeping jet. A double lobe is visible along the axis orthogonal to the direction of the sweeping motion (i.e., z-axis). This might be due to geometrical defects of the device caused by the 3D printing technology and by a potential imperfect alignment between the two symmetrical parts of the actuator.

During the cycle, the jet sweeps from the right side to the left side of the flow field; specifically, it is possible to see that at $\phi = 0°$ the jet is on the right side of the field, while at $\phi = 120°$ the jet is in the process of sweeping to the opposite side. At $\phi = 180°$ the jet is halfway through the cycle, it reaches the left side and afterwards it comes back to the starting position.

Since the results of the phase-averaged Nusselt number distributions over the foil are similar for the nozzle-to-plate distances $H/w = 4, 6$ and 8, for brevity, only the results obtained for $H/w = 6$ have been illustrated.

In Figure 7 the phase-averaged Nusselt number for the nozzle-to-plate distance $H/w = 6$ is represented.

From the analysis of Figure 7 it is possible to observe that the maximum values of the Nu_ϕ are lower than the ones assumed at $H/w = 2$. Furthermore, during the jet transition phases the values of the Nu_ϕ are lower than the values assumed at the extreme points reached by the sweeping jet; this could be due to the high speed of the oscillation in these phases, which does not allow an efficient convective heat transfer.

In the Nu_ϕ maps at $H/w = 6$, an elongated shape of the region of higher Nu_ϕ can be seen; this may be due to a larger spread of the jet into the surrounding environment, caused by a higher nozzle-to-plate spacing. Indeed, higher
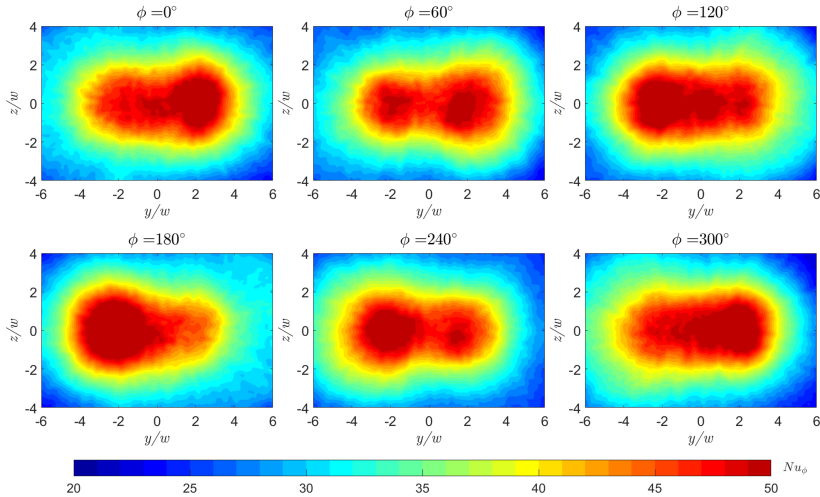
Fig. 7:   Phase-averaged Nusselt number maps for $H/w = 6$, $L_f/w = 4.5$, $Re = 2.16 \times 10^4$.

H/w values allow the jet to reach extremal positions along the axis of oscillation (y-axis) further from the impingement centre, resulting in the formation of two regions of maximum convective heat transfer, the positions of which are almost symmetrical with respect of the impingement centre, in agreement with the results found by Zhou et al. [8] and by Agricola et al. [20].

From the analysis of the results obtained it has been possible to observe that at low nozzle-to-plate distances ($H/w < 4$), the flow impinging the plate causes high heat transfer in the impingement central area, while at higher distances ($H/w \geq 4$), the impingement flow widely spreads into the surrounding environment, causing a convective heat transfer pattern with maximum values of the Nusselt number in the extremal areas of the plate. This phenomenon might be due to the fact that the oscillation of the jet is not limited by the plate as H/w increases and this implies a different organization of the oscillations, which leads to higher values of the Nusselt number in the extremal areas along the direction of the oscillation.

Furthermore, while for $H/w = 4, 6$ and 8 the transition phase from an extremal position to the other is clearly visible, for $H/w = 10$ (see Figure 8) the Nu_ϕ maps have localized spots on the right and on the left with respect of the impingement centre during the same phase. This phenomenon might be due to the fact that increasing the nozzle-to-plate distance the coherence of the oscillating phenomenon is lost and the impinging flow field results from the superposition of a time-averaged component and of a random turbulent fluctuation only.

In Figure 9 the maps of the time-averaged Nusselt number $\overline{Nu}$ at the non-dimensional nozzle-to-plate distances H/w equal to $2, 4, 6, 8$ and 10 are illustrated.
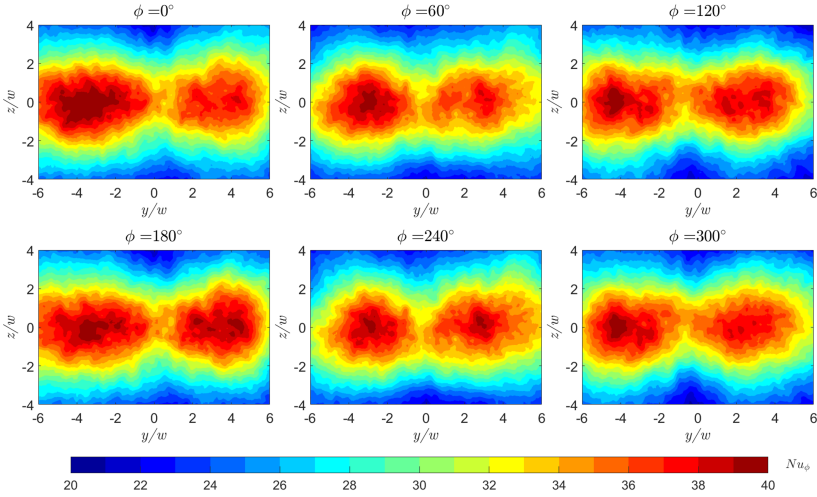
Fig. 8: Phase-averaged Nusselt number maps for $H/w = 10$, $L_f/w = 4.5$, $Re = 2.16 \times 10^4$.
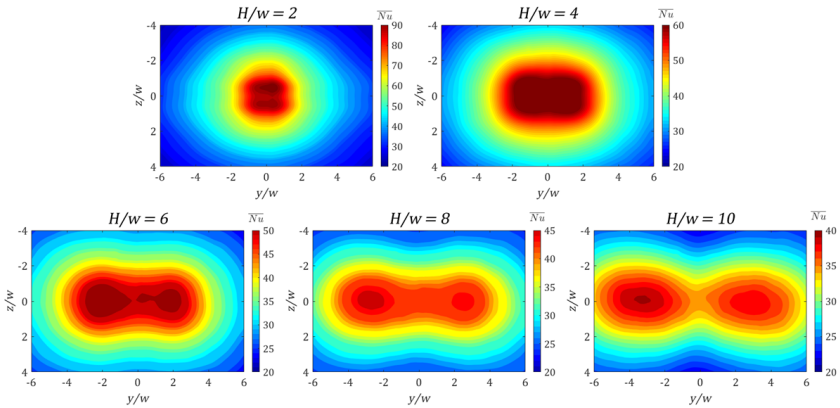

Fig. 9: Time-averaged Nusselt number for $H/w = 2, 4, 6, 8, 10$, $L_f/w = 4.5$, $Re = 2.16 \times 10^4$

At $H/w = 2$, it is possible to observe a central zone with higher $\overline{Nu}$ which is slightly elongated in the direction of the oscillation of the sweeping jet. As the nozzle-to plate distance increases, the Nusselt number values decrease. Indeed, due to the momentum diffusion, increasing H/w the jet velocity reduces, resulting in a decrease of the maximum phase-averaged and time-averaged Nusselt number values. It is also possible to see that, increasing the nozzle-to plate distance, the distribution of the Nusselt number drastically changes; indeed, for $H/w \geq 6$ two lobes can be seen in the direction of the jet oscillation. In

fact, greater nozzle-to-plate spacings allow the jet to diffuse in the surrounding environment, leading to enhanced heat transfer performances in the region of the foil far from the impingement centre.

Furthermore, an asymmetry with respect to the axis perpendicular to the direction of the oscillation in the $\overline{Nu}$ distributions is notable; this is probably due to geometric internal asymmetries of the device.

4.2 Effects of the mixing chamber length

In the current section the effect of the mixing chamber length on the heat transfer performances of impinging sweeping jets has been analysed. As previously said, the heat transfer performances of two sweeping jet devices, characterized by different mixing chamber lengths, have been investigated.

Differently from the configuration characterized by a mixing chamber length equal to $L_f/w = 4.5$, at lower mixing chamber length L_f, no oscillation has been detected in the phase-averaged Nusselt number distribution; therefore, only time-averaged analysis have been performed for the device having $L_f/w = 2.5$. Indeed, for the shorter sweeping jet actuator no coherent oscillation could be detected from the analysis of the pressure signal.

In Figure 10, the time-averaged Nusselt number distributions for non-dimensional nozzle-to-plate distances H/w ranging between 2 and 10 are represented for the device having $L_f/w = 2.5$.
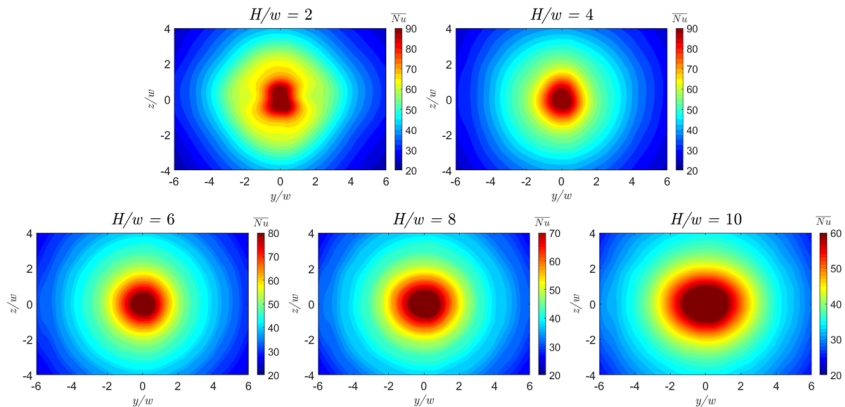

Fig. 10: Time-averaged Nusselt number for $H/w = 2, 4, 6, 8, 10$, $L_f/w = 2.5$, $Re = 2.16 \times 10^4$.

The region with the maximum convective heat transfer does not have an elongated shape along the horizontal axis, but it is characterized by a circular lobe located at the centre of the impinging plate, except for $H/w = 2$. At this distance, indeed, a sort of double lobe in the vertical direction can be identified; this phenomenon might be due to geometrical defects of the device, as

previously explained for the device with the longer mixing chamber. Further-more, with the increase of the nozzle-to plate distance, it is possible to observe that the circular pattern tends to assume an elliptical shape; this may be due to the fact that there is still a preferential direction in the jet spreading caused by the diverging geometrical characteristic of the exit nozzle.

As for the device having $L_f/w = 4.5$, it is possible to notice that the increase of the nozzle-to plate distance causes the Nusselt number values to decrease. In Figure 11 the values assumed by the Nusselt number along the axis of the oscillation for the two analysed devices are depicted; it is possible to observe that, compared with the device characterized by $L_f/w = 4.5$, the device which has $L_f/w = 2.5$ allows to have a greater convective heat trans-fer at the impingement centre for non-dimensional nozzle-to-plate distances $H/w > 2$. Nevertheless, the device with the longer mixing chamber provides heat transfer at higher distances along the direction of the oscillation due to a wider spreading of the jet for non-dimensional nozzle-to-plate distances $H/w > 2$.
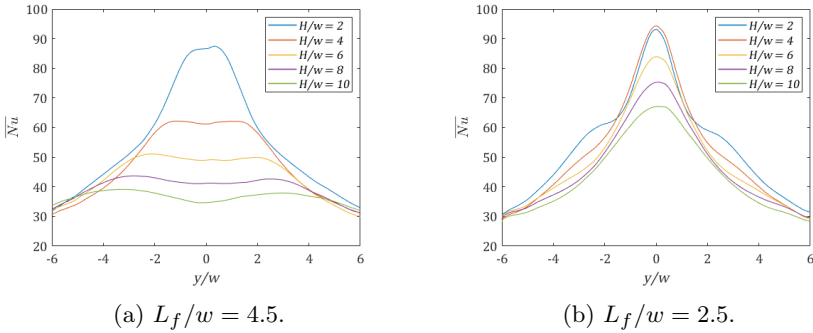

(a) $L_f/w = 4.5$.   (b) $L_f/w = 2.5$.

Fig. 11: Behaviour of $\overline{Nu}$ with y/w for $H/w = 2, 4, 6, 8, 10$.

4.3 Effects of the feedback channel head loss

The main aim of the current section is to investigate the effect of the head loss on the convective heat transfer behaviour of the device having $L_f/w = 4.5$ by fastening the screws into the tapped holes in order to reduce the section of the feedback channel. The same nozzle-to-plate distances ($H/w = 2, 4, 6, 8$, and 10) have been tested for different values of the g/w parameter. The configuration with $g/w = 1$ has already been analysed, therefore the results obtained for the other values of the parameter g/w will be discussed in comparison with the results obtained for $g/w = 1$.

It was observed that the evolution of the phase-averaged Nusselt number over an oscillation cycle for the case $g/w = 0.83$ is very similar to the evolution previously analysed for the case $g/w = 1$. Therefore, since the results obtained

for $g/w = 0.83$ exhibit many similarities with the results obtained for $g/w = 1$, the former are not here reported.

From the analysis of the results obtained for $g/w = 0.67$ it is remarkable the evolution of the phase-averaged Nu_ϕ for 6 phases at the nozzle-to-plate distance $H/w = 4$, depicted in Figure 12.
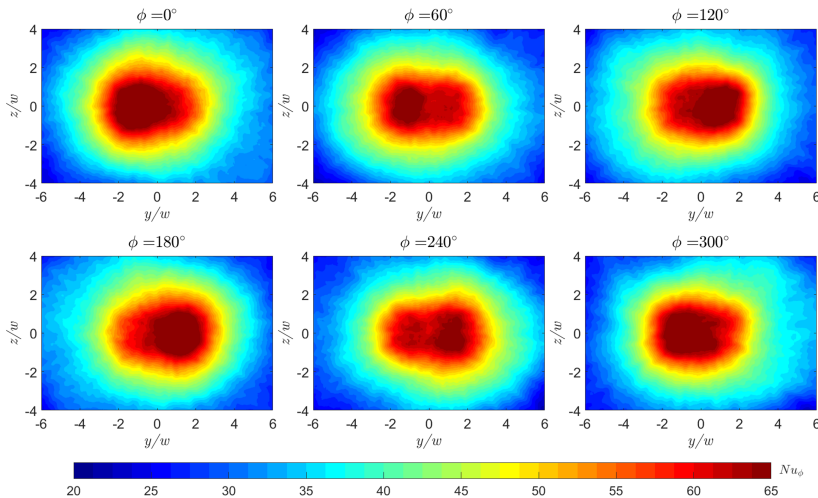

Fig. 12: Phase-averaged Nusselt number maps for $H/w = 4$, $L_f/w = 4.5$, $g/w = 0.67$, $Re = 2.16 \times 10^4$.

Indeed, there are no significant differences in the maximum and minimum values assumed by the phase-averaged Nu_ϕ in comparison with the case $g/w = 1$, while it is possible to note that the elongation of the region characterized by higher values of the Nusselt number is lower than the one relative to the case of $g/w = 1$. Therefore, it is remarkable that by increasing the head losses the spreading of the jet into the surrounding environment decreases.

Furthermore, for $H/w \geq 8$ and for $g/w = 0.67$ it has not been possible to detect a clear oscillation in the phase-averaged Nusselt number snapshots.

For the case $g/w = 0.50$, it has been possible to detect an oscillation in the phase-averaged Nusselt number only for the nozzle-to-plate distance $H/w = 2$. For greater nozzle-to-plate spacings no clear oscillation could be detected in the phase-averaged Nusselt number distribution.

From the configuration characterized by $g/w = 0.50$ and $H/w = 2$, when decreasing the g/w value or increasing the H/w one (or both), it has not been possible to detect a clear oscillation in the phase-averaged Nusselt number distribution; therefore, only time averaged analysis have been performed in order to investigate the effect of the g/w parameter on the heat transfer performances of impinging sweeping jets.

In particular, in Figure 13 the values assumed by the time-averaged Nusselt number $\overline{Nu}$ along the axis of the oscillation for the analysed values of g/w and for $H/w = 2$ and 6 are depicted; furthermore, the values of $\overline{Nu}$ for the device having $L_f/w = 2.5$ have been also depicted.
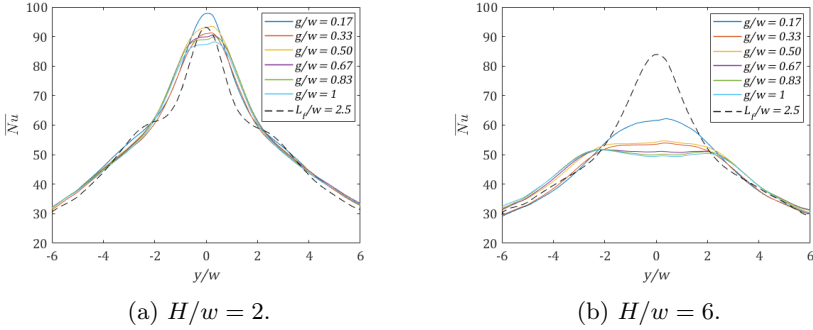

(a) $H/w = 2$.   (b) $H/w = 6$.

Fig. 13: Behaviour of $\overline{Nu}$ with y/w for $g/w = 0.17, 0.33, 0.50, 0.67, 0.83, 1$ ($L_f = 4.5$) and for $L_f = 2.5$.

From the analysis of Figure 13 it is possible to notice that the maximum values assumed by the time-averaged Nusselt number for $g/w = 0.17$ are greater than the ones obtained for all the other values of g/w, at each nozzle-to-plate spacing. Furthermore, from the comparison of the values assumed by $\overline{Nu}$ for the device with $L_f/w = 2.5$ and for the one with $L_f/w = 4.5$ at different head losses conditions, it is possible to point out that for $H/w = 6$ the values of $\overline{Nu}$ near the impingement centre for the device with $L_f/w = 2.5$ are greater than the ones for the device with $L_f/w = 4.5$; this behaviour is opposite to the one observable for $H/w = 2$. Indeed, in the latter case the greatest values of $\overline{Nu}$ near the impingement centre are generated by the device with $L_f/w = 4.5$ and $g/w = 0.17$; this result is in agreement with the results obtained by Park et al [7], who found out that a sweeping jet shows superior capability of heat transfer if compared to a steady jet for $H/w = 1$ and for a fluidic oscillator characterized by an exit nozzle angle of $100°$ and by an aspect ratio $AR = 1$.

Another effect of the increase of the head losses concerns the $\overline{Nu}$ distribution. Further in details, as the g/w value decreases, the dimensions of the single circular lobe of the maximum convective heat transfer at the impingement centre of the plate progressively reduces for all the values of the non-dimensional spacings H/w.

Moreover, from the comparison of the time-averaged Nusselt number distributions over the foil at $H/w = 8$ and at $H/w = 10$ for the different values of g/w considered it is noteworthy that by increasing the head losses the two typical lobes of the $\overline{Nu}$ distributions gradually approach to each other until, for $g/w = 0.17$ the two lobes tend to merge, thus generating a sort of an elliptical shape which develops along the direction of the oscillation. Indeed, it is

possible to observe that the increase of the head losses causes a decrease of the spreading of the jet in the direction of oscillation over the plate.

From the analysis of the spectrogram of the pressure signal (see Figure 14) it has been possible to determine the most probable frequency of the sweeping oscillation; it has been found that with the increase of the head losses the frequency of the oscillation f_0 increases. This result is contradictory to the results obtained by Bobusch et al. [17], who found that the increase of the pressure loss across the feedback channels determines a decrease of the oscillation frequency.
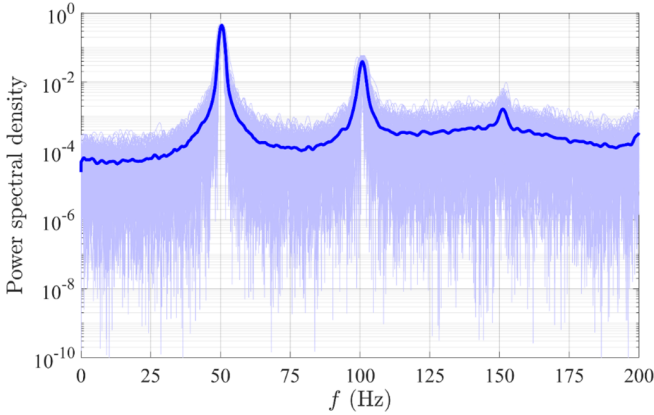

Fig. 14: Spectrogram of the pressure signal for $L_f/w = 4.5$.

5   Conclusions

In the current work the influence of the nozzle-to-plate distance, of the mixing chamber length and of the feedback channel head loss over the heat transfer performances of impinging sweeping jets have been analysed.

Time-averaged and phase-averaged analyses have been carried out in order to characterize the heat transfer behaviour of the sweeping jets.

From the analysis of the results obtained it has been possible to deduce that the increase of the nozzle-to-plate distance causes a decrease of the values assumed by the Nusselt number and that the distribution of the Nusselt number over the plate drastically changes.

As regards the influence of the mixing chamber length, it has been possible to observe that a too small value of this geometric parameter causes the suppression of the jet oscillation and a consequent variation in the Nusselt number distribution. Furthermore, with respect to the device characterized by $L_f/w = 4.5$, the device which has $L_f/w = 2.5$ allows to have a greater convective heat transfer at the impingement centre for non-dimensional nozzle-to-plate distances $H/w > 2$, whereas the longer device provides greater heat

transfer at higher distances along the direction of the sweeping oscillation for $H/w > 2$.

Analysing the distribution of the Nusselt number over the foil for different conditions of head losses in the feedback channel has allowed to comprehend that by increasing the head losses the spreading of the jet into the surrounding environment decreases. Furthermore, it has been found that for $g/w < 0.5$ and for $H/w > 2$ no clear oscillation could be detected in the phase-averaged Nusselt number distribution; therefore, only time averaged analysis have been performed for these configurations in order to investigate the effect of the g/w parameter on the heat transfer performances of impinging sweeping jets. Moreover, it has been possible to notice that the maximum values assumed by the time-averaged Nusselt number for $g/w = 0.17$ are greater than the ones obtained for all the other values of g/w, at each nozzle-to-plate spacing. Finally, from the analysis of the spectrogram of the pressure signal it has been found that with the increase of the head losses the sweeping oscillation frequency increases.

References

[1] J. Seo, C. Zhu, R. Mittal, Flow physics and frequency scaling of sweeping jet fluidic oscillators. AIAA Journal **56**(6), 2208–2219 (2018)

[2] B.C. Bobusch, R. Woszidlo, J. Bergada, C.N. Nayeri, C.O. Paschereit, Experimental study of the internal flow structures inside a fluidic oscillator. Experiments in fluids **54**(6), 1–12 (2013)

[3] K. Jambunathan, E. Lai, M. Moss, B. Button, A review of heat transfer data for single circular jet impingement. International journal of heat and fluid flow **13**(2), 106–115 (1992)

[4] D. Lytle, B. Webb, Air jet impingement heat transfer at low nozzle-plate spacings. International Journal of Heat and Mass Transfer **37**(12), 1687–1697 (1994)

[5] R.K. Lundgreen, M.A. Hossain, R. Prenter, J.P. Bons, J.W. Gregory, A. Ameri, Impingement heat transfer characteric of a sweeping jet. 55th AIAA Aerospace Sciences Meeting p. 1535 (2017)

[6] X. Wen, Y. Liu, H. Tang, Unsteady behavior of a sweeping impinging jet: Time-resolved particle image velocimetry measurements. Experimental Thermal and Fluid Science **96**, 111–127 (2018)

[7] T. Park, K. Kara, D. Kim, Flow structure and heat transfer of a sweeping jet impinging on a flat wall. International Journal of Heat and Mass Transfer **124**, 920–928 (2018)

[8] W. Zhou, L. Yuan, Y. Liu, D. Peng, X. Wen, Heat transfer of a sweeping jet impinging at narrow spacings. Experimental Thermal and Fluid Science **103**, 89–98 (2019)

[9] L. Taubert, I. Wygnanski, Preliminary experiments applying active flow control to a 1/24 th scale model of a semi-trailer truck. The Aerodynamics of Heavy Vehicles II: Trucks, Buses, and Trains pp. 105–113 (2009)

[10] R. Seele, P. Tewes, R. Woszidlo, M.A. McVeigh, N.J. Lucas, I.J. Wygnanski, Discrete sweeping jets as tools for improving the performance of the v-22. Journal of Aircraft **46**(6), 2098–2106 (2009)

[11] G. Raman, S. Raghu, Cavity resonance suppression using miniature fluidic oscillators. AIAA journal **42**(12), 2608–2612 (2004)

[12] D. Guyot, B. Bobusch, C.O. Paschereit, S. Raghu, Active combustion control using a fluidic oscillator for asymmetric fuel flow modulation. 44th AIAA/ASME/SAE/ASEE Joint Propulsion Conference & Exhibit p. 4956 (2008)

[13] D. Thurman, P. Poinsatte, A. Ameri, D. Culley, S. Raghu, V. Shyam, Investigation of spiral and sweeping holes. Journal of turbomachinery **138**(9), 091,007 (2016)

[14] R. Woszidlo, F. Ostermann, H.J. Schmidt, Fundamental properties of fluidic oscillators for flow control applications. AIAA Journal **57**(3), 978–992 (2019)

[15] R. Woszidlo, H. Nawroth, S. Raghu, I. Wygnanski, Parametric study of sweeping jet actuators for separation control. 5th flow control conference p. 4247 (2010)

[16] R. Woszidlo, F. Ostermann, C.N. Nayeri, C.O. Paschereit, The time-resolved natural flow field of a fluidic oscillator. Experiments in fluids **56**(6), 1–12 (2015)

[17] B.C. Bobusch, R. Woszidlo, O. Krüger, C.O. Paschereit, Numerical investigations on geometric parameters affecting the oscillation properties of a fluidic oscillator. 21st AIAA computational fluid dynamics conference p. 2709 (2013)

[18] H. Viets, Flip-flop jet nozzle. AIAA journal **13**(10), 1375–1379 (1975)

[19] J.W. Gregory, J.P. Sullivan, G. Raman, S. Raghu, Characterization of the microfluidic oscillator. AIAA journal **45**(3), 568–576 (2007)

[20] L. Agricola, R. Prenter, R. Lundgreen, M. Hossain, A. Ameri, J. Gregory, J. Bons, Impinging sweeping jet heat transfer. 53rd AIAA/SAE/ASEE Joint Propulsion Conference p. 4974 (2017)

[21] W.C. Horne, N. Burnside, Acoustic study of a sweeping jet actuator for active flow control (afc) applications. 22nd AIAA/CEAS Aeroacoustics Conference p. 2892 (2016)

[22] T. Astarita, G. Cardone, G. Carlomagno, C. Meola, A survey on infrared thermography for convective heat transfer measurements. Optics & Laser Technology **32**(7-8), 593–610 (2000)

[23] G.M. Carlomagno, L. de Luca, Infrared thermography in convective heat transfer. Handbook of flow visualization pp. 547–575 (2018)

[24] T. Astarita, G.M. Carlomagno, *Infrared thermography for thermo-fluid-dynamics* (Springer Science & Business Media, 2012)

[25] C.S. Greco, G. Paolillo, A. Ianiro, G. Cardone, L. De Luca, Effects of the stroke length and nozzle-to-plate distance on synthetic jet impingement heat transfer. International Journal of Heat and Mass Transfer **117**, 1019–1031 (2018)